ARTICLE

Check for updates

3D test sample for the calibration and quality control of stimulated emission depletion (STED) and confocal microscopes

Ernest B. van der Wee [1,2,5], Jantina Fokkema[1,5], Chris L. Kennedy[1], Marc del Pozo [1,3],
D. A. Matthijs de Winter[1,4], Peter N. A. Speets [1,2], Hans C. Gerritsen[1] & Alfons van Blaaderen [1✉]

Multiple samples are required to monitor and optimize the quality and reliability of quantitative measurements of stimulated emission depletion (STED) and confocal microscopes. Here, we present a single sample to calibrate these microscopes, align their laser beams and measure their point spread function (PSF) in 3D. The sample is composed of a refractive index matched colloidal crystal of silica beads with fluorescent and gold cores. The microscopes can be calibrated in three dimensions using the periodicity of the crystal; the alignment of the laser beams can be checked using the reflection of the gold cores; and the PSF can be measured at multiple positions and depths using the fluorescent cores. It is demonstrated how this sample can be used to visualize and improve the quality of STED and confocal microscopy images. The sample is adjustable to meet the requirements of different NA objectives and microscopy techniques and additionally can be used to evaluate refractive index mismatches as a function of depth quantitatively.

[1] Soft Condensed Matter and Molecular Biophysics, Debye Institute for Nanomaterials Science, Utrecht University, Utrecht, the Netherlands. [2] Present address: Department of Imaging Physics, Delft University of Technology, Delft, the Netherlands. [3] Present address: Stimuli-responsive Functional Materials and Devices, Department of Chemical Engineering, Eindhoven University of Technology, Eindhoven, the Netherlands. [4] Present address: Environmental Hydrogeology, Department of Earth Sciences, Utrecht University, Utrecht, the Netherlands. [5] These authors contributed equally: Ernest B. van der Wee, Jantina Fokkema. ✉email: a.vanblaaderen@uu.nl

Reliable quantitative 3D light microscopy measurements require a well-calibrated setup. Moreover, proper alignment of the microscope contributes to higher resolving power, thereby enabling analysis at a smaller scale[1]. Calibration and alignment have become even more critical with the advent of super-resolution microscopy techniques, such as stimulated emission depletion (STED) microscopy[2–4]. In addition, it has been demonstrated that image restoration with an experimentally measured point spread function (PSF) allows for better image restoration than deconvolution with a theoretical PSF[1,5–8]. Measurements of the PSF in 3D are also of importance if one wants to achieve the maximum possible accuracy in the analysis of microscopy images[9,10]. Therefore, it is important to be able to reliably measure the PSF in 3D of a microscope setup, in combination with a proper alignment and calibration in all three dimensions.

Currently, multiple samples and methods are needed for a complete evaluation of a light microscopy setup that is to be used for quantitative measurements. First of all, calibration of the microscope in the lateral directions can be performed with commercially available stage micrometers. For the calibration in the axial direction, various methods have been reported including the use of tilted patterns[11,12], clusters of silica beads[13], large spherical beads with a fluorescent coating, and glass cells calibrated by light interference[14]. The resolving power and illumination uniformity of a light microscope system can be monitored using laser-written slides. These slides are commercially available[15] or have been reported in literature[16], but they are incompatible with STED microscopy. The alignment of excitation beams is commonly checked with <100 nm gold beads[17]. The same gold beads can be used to check the alignment of the depletion beam with the excitation beam of a STED microscope, which is crucial to maximize the performance of the system[17].

Measurements of the PSF of a confocal microscope can be performed by imaging sub-diffraction sized (<175 nm in diameter) fluorescent beads[18] or larger beads in combination with deconvolution software[14]. Smaller beads are required for STED microscopy, as the size of the fluorescent probes (<50 nm in diameter) need to be close, or below the resolving power. For this, brighter beads have become commercially available in recent years, allowing for the evaluation of the resolving power of a STED setup[19]. Furthermore, DNA origami nanorulers have proven to be suitable probes for evaluating STED resolving powers[19–21]. As the spacing between multiple fluorescent centers in the nanorules can be controlled, the resolving power can easily be assessed in both the lateral[19,20] and axial direction[22]. In addition, multiple fluorophores can be combined in a single DNA origami structure[21]. Finally, it has been demonstrated that photostable quantum dots can be imaged with STED[23,24] and could therefore be used as fluorescent probes for PSF measurements of a STED microscope. However, a simple method to ensure enough separation between the quantum dots in 2D or a method to produce more extensive 3D samples is not yet available.

While the quality control methods used so far are good tools to check the performance of a microscope, these methods usually apply to measurements close to the cover glass or are embedded in a high refractive index medium (>1.52)[15,16]. Super-resolution imaging far from the cover glass was demonstrated in life science specimens, where the refractive index is around to 1.45, using (3D) STED in combination with glycerol objectives[1,25,26]. Therefore, it would be beneficial to have a 3D sample with a similar refractive index. In addition, knowledge of the depth-dependent PSF is shown to be important for accurate 3D image reconstruction[8] and high accuracy image analysis[9,10].

Here, we present a single sample for the 3D calibration and alignment, as well as the PSF measurement of a confocal (STED) microscope. The sample is composed of a colloidal crystal consisting of a mixture of highly monodisperse silica beads with gold or fluorescently labeled silica core. The crystal is refractive index-matched with an embedding solvent mixture, resulting in optimal imaging conditions and an effective refractive index similar to life science specimens optimized for glycerol objectives. The periodicity of the crystal in the lateral and axial directions is used as a ruler to perform calibrations. The gold cores are used to image the excitation and depletion spots in reflection and to align the STED microscope. The fluorescent cores are individually resolvable as they are separated by a non-fluorescent silica shell and can therefore be used for PSF measurements at different positions and depths in the sample. By ensuring that the particles with the different cores have the same total size and the same inter-particle interactions, the resulting colloidal crystals are solid solutions of the different types of core-shell particles on the close-packed lattices.

Results

The sample. The sample used for calibration, alignment, and PSF measurement is depicted in Fig. 1. The sample is composed of silica beads with an average diameter of 505 nm (<2% polydispersity index (PDI), where PDI is the standard deviation over the average diameter) that are assembled into a colloidal crystal on a cover glass by vertical deposition[27]. The thickness of the crystal can be tuned by performing repeated deposition steps or by varying the concentration of particles during deposition. The cores of the silica beads consist of either gold (80 nm in diameter) or rhodamine B fluorescently labeled silica (45 nm in diameter). The number ratio between the two types of particles was chosen to be approximately 1–100, respectively.

To characterize the structure of the sample, a crystal was grown using the same method, but with slightly larger particles and was imaged using focused ion beam scanning electron microscopy (FIB-SEM) tomography[28,29] (see Supplementary Note 1). From the recorded FIB-SEM data the coordinates of the particles were
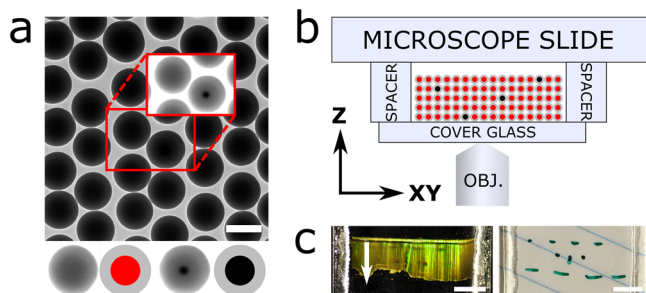

Fig. 1 Calibration and alignment sample. a Transmission electron micrograph (TEM) of the two building blocks of the sample: monodisperse silica-coated 45 nm fluorescent silica (red) and 80 nm gold (black) cores with a total diameter of 505 nm. The bottom row depicts the fluorescent (left two) and gold core (right two) particles, as imaged with TEM (left) and as schematic (right) as used in (**b**). The cores of the schematic particles are not drawn to scale. Inset: upon (TEM) contrast variation the gold cores become visible. The scale bar is 500 nm. **b** Schematic of the sample as seen from the side consisting of a crystal composed of the particles in (**a**). **c** Top view of the sample showing the bright Bragg reflections of the index matched crystal upon illumination from the side (left) and full transparency under available light (right). The green marking on the sample was used to locate the crystal after refractive index matching. The direction of crystal growth during vertical deposition is parallel to the Y direction, as indicated by the white arrow in (**c**). The scale bars are 0.5 cm.
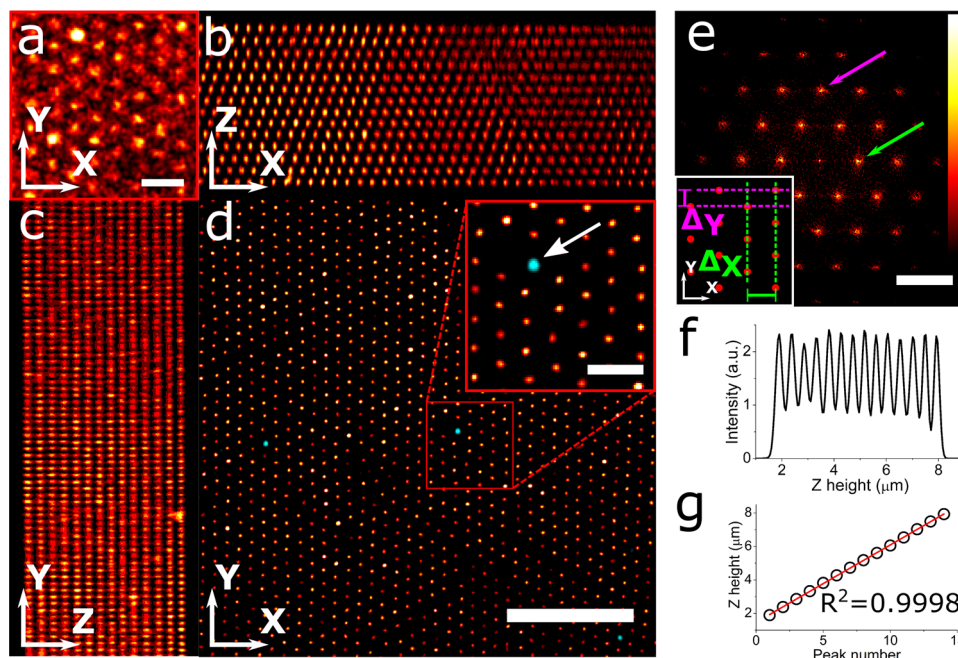
Fig. 2 Calibration of confocal microscope. a Close-up of a slice 3.6 μm from the cover glass from a confocal stack of the colloidal crystal (1 pixel Gaussian blur) acquired using a Leica HC PL APO 93×/1.30 GLYC motCORR STED WHITE objective and a pinhole of 0.7 Airy units. The scale bar is 1 μm. **b** Average projection of the *XZ* planes of the confocal *Z*-stack after deconvolution, showing the ABC stacking in the ($\bar{1}$10) plane of the FCC crystal. **c** Average projection of the *YZ* planes of the deconvolved confocal *Z*-stack, showing the (11$\bar{2}$) plane of the FCC crystal. **d** Overlay of an *XY* slice of the confocal stack of both reflection (cyan) and deconvolved fluorescence (red) 3 μm from the cover glass. The arrow points at a gold core bead imaged in reflection mode. The scale bars are 5 and 1 (inset) μm. **e** Fast Fourier transform of (**d**) demonstrating long-range hexagonal order. The arrows point to the peaks in the FFT image used for calibrating distances in the *X* (green) and *Y* (magenta) directions. The scale bar is 3 μm^{-1}. The inset shows the characteristic distances Δ_X (green) and Δ_Y (magenta) in the real-space crystal corresponding to the peaks in the FFT image. **f** Intensity profile in the *z*-direction, demonstrating the periodicity in the axial direction. **g** Linear fit of the peak positions in (**f**).

determined, as described in ref.[29] (see Supplementary Fig. 1). From the coordinates, we could identify the crystal structure as face-centered cubic (FCC) with stacking faults of hexagonal close-packed (HCP) order using bond orientational order parameters[30]. We also observed that the hexagonal arrangement of the particles in the (111) plane of the FCC crystal is not perfectly hexagonal. In the direction of crystal growth (*Y* in Fig. 1c) the distance to the nearest neighbor was ~4% smaller than in the two other nearest neighbor directions of the hexagon. This is in agreement with earlier studies using X-ray diffraction and FIB-SEM tomography where a similar crystal growth method was used[29,31]. This slightly anisotropic deformation of the close-packed layers is almost certainly caused by the strong capillary forces between the drying liquid and the particles and the orientation of the layers with respect to the drying front. In addition, the layer spacing of the crystal perpendicular to the (111) plane was constant throughout the crystal (see Supplementary Fig. 1d, e).

The sample was prepared from the crystal as follows. The cover glass with the crystal was glued onto two glass spacers fixed onto a microscope slide (Fig. 1b). To suppress scattering during imaging of the sample and distortions of the PSF, the crystal was infiltrated with a refractive index matching solvent mixture composed of glycerol and *n*-butanol ($n_D^{21} = 1.4286$, Supplementary Note 2). After infiltration, the sample was fully transparent under available light, whereas bright Bragg reflections were observed upon illumination from the side (Fig. 1c). The sample was sealed using UV glue. In our experience, samples prepared in this manner have a shelf life of at least 3 years.

Lateral and axial calibration. A *Z*-stack of the silica beads with rhodamine B labeled cores was recorded in fluorescent mode using a Leica HC PL APO 93×/1.30 GLYC motCORR STED

WHITE objective (Fig. 2a). The periodicity of the crystal in both the lateral as well as the axial direction becomes visible after deconvolution of the *Z*-stack (Fig. 2b–d). The (111) plane of the FCC crystal is parallel to the lateral plane, while the ($\bar{1}$10) and (11$\bar{2}$) planes are parallel to the *XZ* and *YZ* directions, respectively, of the confocal *Z*-stack. The growth direction of the crystal was parallel to the *Y* scanning direction of the confocal microscope. In Fig. 2b a fading of the intensity in the *X* direction is visible, which is due to the presence of a grain boundary in the crystal within the volume of the *Z*-stack. We found that the grain boundary does not significantly influence the calibration measurements as described below.

For calibration in the lateral direction the Fast Fourier transforms (FFT) were calculated of three *XY* slices from the deconvolved 3D confocal stack, respectively 1.3, 3.6, and 5.9 μm away from the cover glass. Figure 2e shows the FFT of the *XY* slice 3.6 μm away from the cover glass, with the arrows pointing at two characteristic distances in the (111) crystal plane in both the *X* (green) and *Y* (magenta) directions (see inset for the corresponding distances in real-space). From the three slices, the characteristic distances Δ_X and Δ_Y were determined to be 481 ± 4 nm and 269 ± 2 nm, respectively. These values can be used to calibrate the two lateral directions of the microscope. Since the hexagonal arrangement is slightly distorted in the direction of crystal growth, *Y* in this case, the orientation of the hexagonal arrangement (and therefore the crystal growth direction) with respect to the confocal scanning direction should be taken into account during the calibration. As the particles are touching in the *Y* direction, the effective particle diameter σ_{eff} can be estimated by $2\Delta_Y$. We find that $\sigma_{eff} = 538 \pm 4$ nm and therefore $\sigma_{eff} \approx 1.07\sigma_{TEM}$. This slightly larger effective diameter compared to the diameter as measured in TEM is expected because the

Confocal

2D-STED
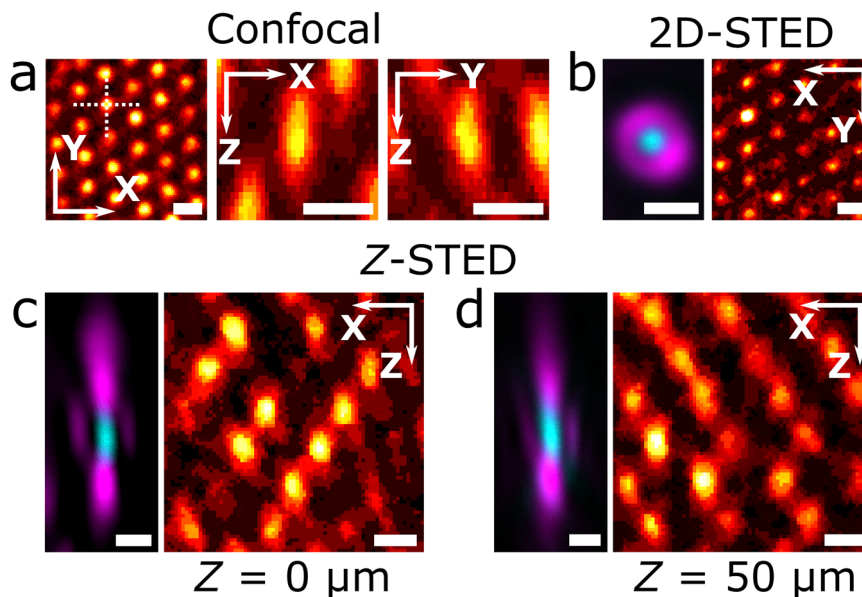

Z-STED

$Z = 0\ \mu m$

$Z = 50\ \mu m$

Fig. 3 Alignment of confocal STED microscope. a Slices from a confocal Z-stack of fluorescent cores in a colloidal crystal close to the cover glass, recorded with a Leica HC PL APO 100×/1.40 OIL STED WHITE objective (2 pixel 3D median filter), showing the response function of the microscope in the lateral plane (left), XZ plane (middle) and YZ plane (right). The two axial planes are marked by the dashed lines in the lateral plane (left). Alignment of 2D-STED (**b**) and Z-STED (**c, d**) excitation (cyan) and depletion (magenta) lasers in the lateral plane, as imaged using a Leica HC PL APO 93×/1.30 GLYC motCORR STED WHITE objective in reflection mode (left) using a gold core particle close to (**b, c**) and 50 μm (**d**) from the cover glass, and the resulting STED images (2 pixel median filter) of the fluorescent cores in the crystal (right), showing increased resolvability of the particles in the crystal as compared to (**a**). Pinhole size in fluorescence images: (**a**) 0.7 and (**b–d**) 1 Airy unit, in all reflection mode images: 4.7 Airy units. All scale bars are 500 nm. Color tables used correspond to those plotted in Fig. 4.

particles shrink due to electron beam exposure during the TEM measurements[32].

For the axial calibration of the setup, the intensity of the deconvolved confocal Z-stack is plotted as a function of the Z height (Fig. 2f). The relative positions of the peaks in this intensity profile display almost perfect linearity ($R^2 = 0.9998$, Fig. 2g) and a linear fit results in a distance of 448 ± 2 nm between the lateral layers of the crystal. It should be noted that axial distances, as recorded by confocal microscopy using high NA objectives, are sensitive to refractive index mismatches between the sample medium and the immersion medium of the objective. This results in an apparent elongation or shrinkage of measured distances[14,33]. The presented sample has a slightly lower refractive index (1.43) than the refractive index of the immersion liquid (1.45). Therefore, the axial scaling factor was determined using the method described by Besseling et al.[14]. A scaling factor of 0.982 ± 0.003 was determined, resulting in a (111) layer spacing d_{111} of the sample of 440 ± 2 nm. For a perfect FCC crystal d_{111} can be calculated using: $d_{111} = \sqrt{6}\sigma/3$, where σ is the particle diameter[31]. Using $\sigma_{eff} = 538 \pm 4$ nm, as estimated before, a value of d_{111} of 439 ± 3 nm is found, which corresponds well to the measured value ($d_{111} = 440 \pm 2$ nm).

PSF measurement and laser beams alignment. Using the fluorescent cores of the beads in the colloidal crystal, the PSF of a confocal microscope can be measured. Figure 3a shows the sub-resolution fluorescent cores close to the coverslip, imaged in confocal mode with a Leica HC PL APO 100×/1.40 OIL STED WHITE objective and the pinhole set to 0.7 Airy units. The PSF of this microscope has an expected ellipsoidal shape in the axial planes, but is also slightly tilted in the YZ plane.

The gold cores in the crystal were used to check the shape of the depletion laser spot and the overlap with the excitation laser

spot, which are both critical for an optimal STED resolving power. Figure 3b shows the excitation spot (cyan) and the 2D-STED[34] 'doughnut'-shaped depletion spot (magenta) imaged in reflection mode using a Leica HC PL APO 93×/1.30 GLYC motCORR STED WHITE objective with the pinhole set to 4.7 Airy units. In 2D-STED the PSF is only improved in the XY plane, contrary to Z-STED where the PSF is (mostly) modified along the optical axis in the Z direction[35]. Subsequent imaging of the fluorescent cores with the pinhole set to 1 Airy unit shows an increase in lateral resolution of the STED microscope (Fig. 3b) as compared to confocal (Fig. 3a), even when using a lower NA objective. The importance of a proper alignment of the STED and excitation lasers is demonstrated in Supplementary Fig. 2, where α-tubulin was imaged using 2D-STED with and without alignment using our sample.

Since 2D-STED microscopy only improves the resolution in the lateral plane compared to confocal microscopy, it is primarily employed on thin samples, close to the cover glass. 3D STED and Z-STED, however, enable imaging at sub-diffraction resolution in both lateral and axial directions also far away from the cover glass and therefore enable imaging thicker samples in 3D at resolutions below the diffraction limit[35]. Figure 3c–d shows the excitation and depletion laser spots of a Z-STED confocal microscope equipped with a Leica HC PL APO 93×/1.30 GLYC motCORR STED WHITE objective as imaged in reflection mode close to the cover glass (Fig. 3c) and ~50 μm away from the cover glass (Fig. 3d) using our sample. The correction collar (CC) of the objective was used to keep the intensity of the top and bottom depletion spots balanced when imaging more than ~30 μm from the cover glass. To check the results of the alignment of the lasers, the fluorescent cores were imaged in Z-STED imaging mode at a pinhole size of 1 Airy unit (Fig. 3c, d). The improved axial resolution of Z-STED imaging is visible from the decreased size of the PSF in the Z direction (FWHM ≈ 300 nm) as compared to the

confocal PSF (FWHM ≈ 600 nm, Fig. 3a), even at ~50 μm away from the cover glass.

The presented sample enables quality control of the PSF, but the measurement of its extended structure requires a greater separation between the fluorescent beads. An increased separation allows imaging of a single bead, without its axial lobes overlapping with those of neighboring particles. Therefore, a slightly modified sample was constructed. This consisted of the same probe particles as described above, arranged not in a dense crystal but sparsely distributed in 3D across a scaffold of unlabeled silica spheres (310 nm, 10% PDI, Supplementary Fig. 3), embedded in a refractive index matching solvent mixture. While shown here in a separate sample, this can also be realized by incorporating sparse spheres with a fluorescently labeled core in the aforementioned crystal (shown in Fig. 1), where the dye of the sparse spheres differs from the dye of the fluorescent particles in the crystal.

Even the slight refractive index mismatch between the immersion and sample media (in this case: 1.45 vs. 1.42) causes increased aberration at increasing imaging depth. This aberration was minimized by attempting to optimize the position of the objective CC using images of the dilute gold-core particles. Two strategies to find this 'optimal' position were tested: maximize the intensity of the excitation reflection (cyan in Fig. 4) or equalize the intensity of the axial Z-STED lobes (magenta in Fig. 4) which become lopsided deep in the sample without CC adjustment (Supplementary Fig. 4). The two strategies were found not to agree on an optimal position, so the latter was chosen to ensure optimal STED imaging. The equalized lobes at each height are shown in the top row of Fig. 4.

By imaging 3D volumes at various heights above the coverslip (using the previously determined CC positions) in both confocal and Z-STED imaging modes, the PSFs shown in Fig. 4 (middle and bottom row) were obtained. Several (>10) beads at each

height were averaged and the PSF at that height was computed by deconvolution with a sphere the size of the fluorescent core[14]. The ability to measure PSFs far from the cover glass was demonstrated using beads at depths up to 100 μm. This enables quality control of the microscope, with this particular setup being found to maintain a compact Z-STED PSF at depths of up to 80 μm. Furthermore, measurements of the PSFs at different heights enable accurate deconvolution and high precision analysis of images captured deep inside thick specimens[8–10].

Discussion

The sample presented here is a robust standard for the quality control of a laboratory's confocal and STED microscopes. The preparation method of the sample ensures a shelf life of at least 3 years. Although the small fluorescent cores tend to bleach upon prolonged excitation the sample can be used repeatedly, as the crystal contains over 10^{10} particles due to its larger size (close to 2 cm^2, see Fig. 1c). The synthesis of the beads requires basic wet lab experience and equipment and has been reproduced twice by co-workers on the basis of the procedure as described in the methods.

During calibration, the characteristic lateral length scales Δ_X and Δ_Y were measured with an error below 1% (obtained by measuring at three depths). In addition, for the axial interlayer spacing an error of less than 0.5% was found (obtained from a linear fit of the intensity peaks of the crystal layers). This low error is supported by the perfect linearity of the axial interlayer spacing as found by FIB-SEM tomography and particle tracking. These low errors make the sample suitable for the calibration of microscopes at high precision.

We have shown how the presented sample can benefit the alignment, calibration, and quality control of STED and confocal microscopes. The sample can also be used for other 3D microscopy techniques capable of optical sectioning. Structured illumination microscopy (SIM) can surpass the resolution of confocal microscopy in samples less than 20 μm thick[36–38]. The small crystal inter-layer distance in the axial direction of ~400 nm in our sample will be too small for 2D SIM, where the lateral resolution is below the diffraction limit and the axial resolution is similar to wide-field microscopy. As there is also an axial resolution improvement in 3D SIM, we believe this sample will allow to image the PSF and calibrate distances in the lateral and axial directions of a 3D SIM microscope. A recently developed microscopy technique, high-NA single objective or oblique plane light-sheet microscopy[39,40] seems compatible with our sample as well. It will allow for the imaging of the PSF throughout the large field of view. Furthermore, the regularity of the sample in all three dimensions may aid in testing the shearing and deconvolution algorithms used in the 3D volume reconstructions[40].

The sample is highly tunable due to the fabrication of the sample by self-assembly of particles into a crystal. This makes it possible to adjust the sample to, for example, meet the requirements for different high NA lenses (e.g. oil immersion) and/or different techniques. This can be achieved by changing the core, the ratio between different types of cores, the refractive index of the particles, the shell, and the total size of the particles, which will be discussed next.

While it was demonstrated that rhodamine B-labeled silica cores can be used, the synthesis method of these cores allows for the incorporation of a wide variety of dyes[41–47]. This can be useful because by mixing cores with different dyes in the non-fluorescent silica growth step, one can accommodate microscope setups with multiple laser lines. Instead of keeping the gold and dye separated within the sample, the two can also be combined within a single particle, by growing a fluorescent layer around the
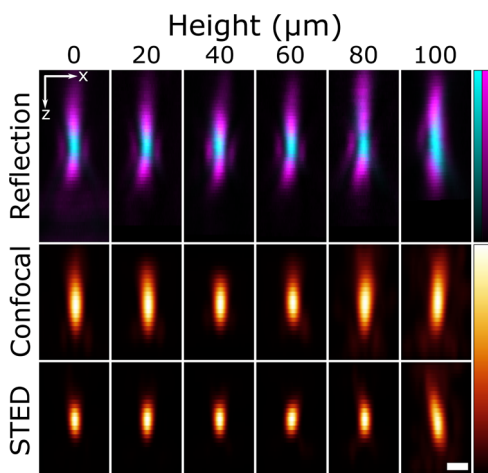

Height (μm)

Fig. 4 Confocal and Z-STED point spread functions at different distances from the coverslip. The excitation (cyan) and depletion (magenta) lasers imaged in reflection using the sparse gold-core particles (top row). To correct for the mismatch between the immersion liquid of the objective and the sample, at every height the correction collar (CC) of the objective was adjusted to equalize the peak intensities of the axial STED lobes (see also Supplementary Fig. 4). Point spread functions in the XZ plane measured in confocal (middle row) and Z-STED (bottom row) mode using silica-coated fluorescent beads dispersed in a disordered scaffold of unlabeled silica spheres (310 nm, 10% PDI, Supplementary Fig. 3). At least 10 well-separated beads were recorded and averaged at each height, and the PSFs were extracted by deconvolution with a sphere the size of the fluorescent cores. The scale bar is 500 nm.

gold core. Another option is to use a silver core instead of a gold core. This flexibility opens up the possibility to design nano-composite particles where the fluorescence is enhanced by the presence of the metal core[48], which has recently been demonstrated to be compatible with STED microscopy[49].

The possibility to exchange the fluorescent cores with quantum dots is also worthwhile exploring, since quantum dots have excellent photostability, are only a few nanometers in size, and have shown to be compatible with STED microscopy[23,24]. As the absorption and emission wavelengths of quantum dots are size dependent[50], they can be tailored to the wavelength of the excitation and STED lasers. When measuring a PSF using quantum dots, the challenge is to ensure there is enough separation between them which can be achieved by coating the quantum dots with silica[51–53]. This seeded growth method is directly compatible with the work presented here, because silica coating is performed in the same reverse micro-emulsion system used to synthesize the fluorescent cores. The most promising quantum dots to use are so-called CdS/CdSe/CdS quantum well dots, as these can be coated with silica while maintaining a high photo-luminescence quantum yield[54,55].

Next to quantum dots, a variety of nanometer-sized probes have been put to use in STED imaging[56], such as fluorescent nanodiamonds[57], upconversion nanocrystals[58], and carbon dots[59]. Although these probes can be coated with silica[60–62], and could be integrated in our demonstrated sample, no STED microscopy has been demonstrated on these probes after silica coating.

Another method to tune the sample is by adjusting the silica shell that is used to ensure separation between the cores. While in this work the focus was on a refractive index of 1.43 compatible with glycerol objectives, it can also be tuned to a higher refractive index. This can be achieved by synthesizing a shell of titania/silica composite with a higher refractive index[63–65]. Doing so, the refractive index can easily be increased to match the refractive index of oil objectives (1.52), or any other intermediate refractive index that is comparable to the refractive index of life science specimens of interest. Another option is to increase the size of the shell to increase the spacing between the probes. This makes the sample compatible with lower NA objectives, where the axial resolving power is smaller. For this, the assembly method needs to be adjusted due to a faster settling rate of the particles, as has been demonstrated for close to 1 µm silica particles[66].

By introducing a refractive index mismatch between the particles and the embedding solvent, the effect of the mismatch on the PSF can be measured as a function of the distance from the cover glass. This allows for the study of aberration corrections using an objective correction collar and a spatial light modulator, which is follow-up work intended from our group. Finally, the periodicity of the crystal in the axial direction and the known refractive indices of the beads and the embedding mixture can be used to test effective medium theories developed to determine an effective refractive index in optically heterogeneous environments[67].

Methods

Particle synthesis: silica-coated gold cores.
Gold nanoparticles (80 nm, in citrate buffer (OD 1), Sigma-Aldrich) were functionalized with polyvinylpyrrolidone (PVP, Mw = 10,000 g mol^{-1}) by transferring 20 mL of the gold nanoparticle solution and 400 µL of a 10% (w/v) PVP solution (1 g in 10 mL water) to a vial[68]. The obtained solution was stirred for 16 h and was transferred to 5 mL eppendorf tubes and centrifuged for 5 min at 5.000 rcf. The supernatant was removed as much as possible with a glass pipette and the gold nanoparticles were redispersed in 2.5 mL ethanol and collected in a 4 mL glass vial.

Silica coating was performed in a closed 4 mL vial under constant stirring at 600 rpm and was initiated by the addition of 250 µL ammonia (28–30 w% NH$_3$ basis, ACS reagent, Sigma-Aldrich) and 25 µL of a 10 vol% solution of tetraethyl

orthosilica (TEOS, reagent grade, 98%) in ethanol (absolute, Merck)[68]. These additions were followed by the addition of 50, 100, and 200 µL of 10 vol% after 90, 270, and 360 min. Total 90 min after the final addition, the solution was transferred to a 20 mL vial and diluted with ethanol to obtain a total volume of 20 mL. This diluted solution was centrifuged for 15 min at 1.000 rcf and the white turbid supernatant was removed. Next, the particles were redispersed in 20 mL ethanol by sonication. Centrifugation and redispersion of the particles were repeated to remove empty silica spheres formed by secondary nucleation. After the final centrifugation step, the particles were redispersed in 10 mL ethanol. The resulting particles and their gold cores were imaged with transmission electron microscopy (TEM) (Supplementary Fig. 5), from which an average particle diameter of 321.5 nm (4.3% polydispersity index (PDI), where PDI is the standard deviation over the average diameter) was determined by measuring 100 particles. In the syntheses we never used TEOS bottles that were open longer than 1 month, as we found these lead to secondary nucleation and aggregates due to the pre-hydrolization of the TEOS[69].

Particle synthesis: silica-coated fluorescent cores.
Dye-APTES coupling was performed by transferring 6.00 mg Rhodamine B isothiocyanate (mixed isomers, RITC, Sigma-Aldrich), 500 µL ethanol, and 12 µL (3-Aminopropyl)triethoxysilane (APTES, 99%, Sigma-Aldrich) to a vial[46,47]. The vial was wrapped in aluminum foil and stirred for 5 h. A reverse microemulsion was prepared by transferring 50 mL cyclohexane (Sigma-Aldrich) and 6.5 mL Igepal CO-520 (Sigma-Aldrich) to a vial under vigorous stirring (700 rpm)[70–72]. As soon as a clear solution was obtained, 400 µL TEOS was added to the solution. After 2 min stirring, 50 µL of the dye-APTES solution was added resulting in the formation of a colorless solution. After an additional 5 min of stirring to ensure complete homogenisation, 750 µL ammonia was added to initiate the reaction. Immediately after this addition, the solution turned pink. After an additional minute of stirring the solution was stored in a dark place for the reaction to proceed. After 24 h, the reaction mixture was transferred to a round-bottomed flask. The cyclohexane was evaporated under reduced pressure (~10mbar) using a rotary evaporator where the flask was placed in a room temperature water bath. It is important that the mixture stays clear during the evaporation of cyclohexane: a mixture turning turbid indicates particles aggregation. After 20 min, a very viscous, pink solution was obtained of fluorescent silica particles dispersed in the non-ionic surfactant. 10 mL N, N-Dimethylfor-mamide (DMF, Sigma-Aldrich), and 10 mL ethanol were added to this liquid resulting in the formation of a clear, non-scattering, pink solution.

As the fluorescent cores have limited stability, we always directly followed the synthesis of the fluorescent cores with further silica growth. To this end, 5.00 mL of the fluorescent core solution, 3.45 mL ethanol, 1.11 mL water, and 0.45 mL ammonia were transferred to a three-necked round-bottomed flask[73–75]. Under gentle stirring (200 rpm) and nitrogen flow, a 3 times diluted solution of TEOS in ethanol was added to the solution using a syringe pump. A water/ammonia/ethanol solution was added simultaneously to keep the water and ammonia concentrations constant. A total of 6.54 mL was added at a flow rate of 0.32 mL/h, after which the flow rate was doubled. After 10.98 mL of TEOS solution was added, the syringes were refilled and TEOS addition was continued until a total volume of 30.13 mL was added. After silica growth, the solution was transferred to two 50 mL eppendorf tubes and centrifuged for 30 min at 2000 rcf. Particles were redispersed in 20 mL absolute ethanol by sonication, collected in one vial, and stored in a fridge at ~4 °C. The resulting particles and their fluorescent cores were imaged using TEM (Supplementary Fig. 6) and the average diameter of the cores and silica-coated particles were 44.7 ± 2.3 and 240.1 ± 4.1 nm, both obtained by measuring the diameter of 100 particles. To match the size of the gold-core silica particles, the fluorescent-core silica particles were grown further. 93 mL ethanol, 1.80 mL of silica-coated fluorescent cores, and 12.4 mL water were transferred to a 250 mL round-bottomed flask. The obtained solution was sonicated for an hour before growth was started. Under gentle stirring (200 rpm) and nitrogen flow, 3 mL of a 3 times diluted solution of TEOS in ethanol was added to the solution using a syringe pump with a flow rate of 0.65 mL/h. A water/ammonia/ethanol solution was added simultaneously to keep the water and ammonia concentrations constant. After this first growth step, a TEM sample was prepared to determine whether the size of the particles matched the size of the silica-coated gold particles.

Particle synthesis: further growth of a mixture of gold- and fluorescent-core particles to 500 nm diameter particles.
Further growth of a mixture of gold- and fluorescent-core silica particles was performed to obtain particles with a total diameter of approximately 500 nm[73–75]. The gold- and fluorescent-core silica particles were mixed in a 1:100 number ratio in ethanol, by adding 8.8 mL of the suspension of silica-coated gold particles to the reaction mixture containing the fluorescent-core silica particles (see the previous paragraph). The concentration of gold particles and the weight fraction of the fluorescent cores were used here to determine how much of the gold-core suspension should be added to obtain the desired 1:100 ratio between the two types of particles. Next, growth was continued by the simultaneous addition of 17.16 mL of the 3 times diluted solution of TEOS in ethanol and the water/ammonia/ethanol solution with a flow rate of 1.00 mL/h. After silica growth, the solution was transferred to three 50 mL eppendorf tubes and centrifuged 30 min at 500 rcf. After repeated centrifugation and redispersion of the particles, all particles were redispersed in 40 mL absolute ethanol by sonication,

collected in one vial, and stored in the fridge. The resulting particle mixture was imaged using TEM (Supplementary Fig. 7), from which the average diameter was determined: 505.1 nm (1.8 % PDI), by measuring 368 particles.

Particle synthesis: non-fluorescent silica particles for scaffolding. Total 15 mL ammonia and 120 g ethanol were mixed in a 250 mL round-bottomed flask and the temperature was raised to 30 °C and stirred using a stir bar[73,76]. To this mixture, 6.60 mL TEOS was pipetted under the liquid surface with vigorous stirring at 600 rpm. After 9 min, blue scattering of the particles was observed and the stirring speed was reduced to 300 rpm. In total 22 h after the TEOS addition, the mixture was poured into a 500 mL centrifuge bottle, ethanol was added and the mixture was centrifuged at 700 g for 45 min. The supernatant was replaced with ethanol and this washing procedure was repeated twice. This resulted in polydisperse particles with a diameter of 310 nm (10% PDI, Supplementary Fig. 3c).

Colloidal crystal growth. Colloidal crystal growth was performed via the vertical deposition method[27] at elevated temperature to speed up the evaporation process[77–79]. Briefly, 8.0 mL of a 1 vol% mixture of gold- and fluorescent-core particles in ethanol with a diameter of ~500 nm was transferred to a 20 mL glass vial. A cover glass (Marienfeld Superior #1.5H, 24 × 50 mm) was placed upright inside the solution under a small angle (~5°) with respect to gravity. This vial, and a 100 mL beaker filled with ethanol were placed inside a 50 °C preheated oven (RS-IF-203 Incufridge, Revolutionary Science) and covered with a large beaker (upside down). After approximately 16 h, the cover glass was removed from the solution. An opaque deposition of particles was observed on the cover glass. Any particles sticking to the back of the cover glass were removed with an ethanol-soaked paper tissue. Bragg reflections were observed which indicates the formation of a crystalline structure. For the growth of thicker crystals, growth steps were performed by repeating the vertical deposition method up to three times. We found that the crystal growth is sensitive to vibrations, caused by the fan present in the oven. After first trying larger ovens, the fan of the smaller Incufridge oven was found to not perturb the crystal growth.

Calibration and alignment sample preparation. Two spacers (Menzel #00 cover glass, thickness = 55–80 μm) were glued onto a microscope slide using UV-glue (Norland 68 Optical Adhesive), about 5 mm apart. Next, the cover glass containing the crystal was glued onto the spacers, such that the crystal was inside the created channel. This channel was then infiltrated with a mixture of n-butanol and glycerol ($n_D^{21} = 1.4286$, measured using an Atago 3T refractometer) in order to refractive index match the particles to the surrounding liquid, to reduce scattering and optimize the imaging conditions (see Supplementary Note 2 and Supplementary Fig. 8). The use of water in the matching solvent mixture was omitted, as it has been reported to change the refractive index of silica particles[80], because it is small enough to enter the interior of the silica network, while molecules larger than 0.3 nm cannot. Finally, the channel was closed using UV-glue. While curing the glue, the crystal was covered with aluminum foil as protection from the UV radiation to prevent bleaching of the dye in the particles.

Confocal and STED measurements. Calibration and alignment measurements were performed on an inverted Leica TCS SP8 STED 3X confocal microscope, equipped with a Leica HC PL APO 100×/1.40 OIL STED WHITE or a Leica HC PL APO 93×/1.30 GLYC motCORR STED WHITE objective with a correction collar (CC). The detection window was selected using an Acousto-Optical Beam Splitter (AOBS). The confocal microscope, as well as the CC were controlled with LAS X software (version 3.5, Leica Microsystems). In the case of the oil objective Type F immersion oil ($n_{546}^{23} = 1.518$, Leica Microsystems) was used as immersion liquid, while for the glycerol objective an 85 w% glycerol/water mixture ($n_D^{20} = 1.452$) was used. To image the fluorescent cores of the particles, a pulsed (80 MHz) super-continuum white light laser (SuperK, NKT Photonics) was tuned at 543 nm, while the emission was detected using a gated (0.3–6.0 ns) HyD detector (553–650 nm). For STED imaging of the fluorescent beads, a continuous wave (CW) depletion laser with a wavelength of 660 nm was used. The depletion laser was either fully focused into a 'doughnut'-shaped spot (2D-STED[34]) or into an axial depletion spot (Z-STED[35]). The gold cores were imaged by detecting the reflection of the excitation or depletion laser using a photomultiplier tube (PMT). The detection range was set with a typical width of 20 nm around the laser wavelength using the AOBS. For confocal microscopes using standard emission filters, the emission filters need to be (manually) removed before reflection imaging. As high reflection intensities can damage the PMT (especially in the case of the high-power STED laser), we used low laser powers for reflection imaging and slowly increased the PMT gain until a signal from the gold beads was detected.

The CC of the glycerol objective was used to compensate for the refractive index mismatch between the sample (1.43) and the objective (1.45) and allowed to fine-tune the depletion laser pattern, as discussed in more detail in the supplementary information of [25]. Acquisition parameters of the confocal and STED images are listed in Supplementary Table 1 and the laser powers used are listed in Supplementary Table 3. Any image filtering was done using Fiji[81] (ImageJ 1.52d).

Image deconvolution. The confocal 3D stack of the fluorescent beads (Fig. 2) was deconvolved with a theoretical point spread function using Huygens Software (Scientific Volume Imaging, 17.04).

Calibration measurements. For the lateral calibration, Fast Fourier transforms of the XY slices were calculated using iTEM (Soft Imaging System GmbH, 5.0) and a 1 pixel Gaussian blur was applied using Fiji[81] to reduce noise. To measure the Δ_X and Δ_Y distances (see Fig. 2e) intensity profiles parallel to the direction of interest were drawn through the origin. Using OriginPro (v8.0891, OriginLab Corporation) Gaussian functions were fitted to the peaks nearest to the origin in the intensity profiles, to obtain the distance of these peaks to the origin Δ_X and Δ_Y.

For the axial calibration, Fiji was used to plot the intensity of the deconvolved confocal Z-stack as a function of Z-height. Using OriginPro the peaks in the profile were fitted with Gaussian functions. The peak positions were plotted as a function of peak number and fitted using a linear function using OriginLab. The slope of this function was used as interlayer distance.

Measuring the scaling factor of a 93×/1.3 NA glycerol objective for $n = 1.43$ samples. To determine the scaling factor of the axial distances in our sample as measured by confocal microscopy, we used the method described in [14]. A sample cell was constructed by gluing two Menzel #00 cover glasses as spacers on a microscope slide, after which a channel was created by bridging the spacers with a Menzel #1.5 cover glass. The Fabry-Pérot fringes were measured using a Fourier-transform infrared (FTIR) spectrometer (Vertex 70, Bruker) and fitted to determine the cell height: 94.257 ± 0.008 μm. Next, rhodamine B dyed poly(methyl methacrylate) spheres (70 nm diameter) were deposited from hexane on the inside of the cell and the height of the cell was measured in fluorescent mode on a confocal microscope equipped with a 20×/0.7 NA air objective: 98.0 ± 0.2 μm, resulting in a miscalibration of the microscope stage of 4.0 ± 0.2%. After filling the cell with the glycerol/n-butanol mixture ($n_D^{21} = 1.4286$) and closing it with UV-glue a height of 99.9 ± 0.2 μm was measured, which was corrected for the miscalibration of the microscope stage: 96.0 ± 0.3 μm. This gives a scaling factor of 0.982 ± 0.003 for axial distances in a sample with a refractive index of 1.43 recorded with a 1.3 NA glycerol objective.

PSF measurement from sparse probe particles. The probe particles in Fig. 1a were distributed in 3D across a scaffold of undyed silica particles. This was achieved by mixing dispersions of the particles in ethanol such that the number ratio of scaffold : fluorescent : gold-core particles was 85000 : 99 : 1. Next, 5 μL of this 18 mg/mL dispersion was repeatedly dropcast on the same spot on a #1.5H cover glass, rapidly evaporating the ethanol in an oven at 50 °C between each drop addition. The resulting residue was uneven with regions more than 100 μm high after several steps. This residue was incorporated into a microscopy cell of the type shown in Fig. 1a (see also Supplementary Fig. 3). The refractive index of the scaffold particles was measured using the method described in Supplementary Note 2 and the cell infiltrated with a liquid mixture of the same refractive index, specifically 63.0 w% glycerol/water ($n_D^{21} = 1.4230$), before sealing with UV-glue.

Before imaging the fluorescent particles, the reflection signals from the gold core particles were used to find optimal parameters for Z-STED imaging. First, the STED alignment was adjusted by centring the excitation and depletion reflection patterns (cyan and magenta respectively in Fig. 4) of a gold-core particle located on the cover glass. Then, a CC position was chosen to equalize the Z-STED axial lobes as viewed in the XZ plane through the centre of the particle. This was achieved by iteratively adjusting the CC position, re-centring the particle in the field of view by moving the sample stage, and checking the intensities of the side lobes with a line profile along Z through the XY centre of the particle. With these equalized as much as possible, the reflection images shown in the top row of Fig. 4 were captured, using the parameters and CC positions in Supplementary Tables 1 and 2, respectively.

Next, image volumes of the fluorescent beads were captured from which to extract the PSFs. At each height, test images using low laser power were captured at different XY positions to discern whether or not any fluorescent beads were located in the region of interest, away from the edges. If so, the position was marked and eventually 7–15 XYZ stacks of dimension 10.4 × 10.4 × 4.1 μm were captured at the various chosen XY positions in a 'Mark and Find' acquisition. The checking was required to avoid wasted image volumes containing no usable particles and it was done in this way to avoid bleaching the fluorescent cores before the main measurement. The low pixel dwell time (0.3 μs) used was to ensure that the beads did not bleach significantly during acquisition. Approximately thirteen image volumes were recorded at each height, each with imaging times of around 1 min. The confocal PSFs were recorded first, followed by the STED ones, with 5 h between the first and last measurements. The room temperature was maintained at 23.5 °C throughout this period.

The beads in the image volumes at each height were located and summed together to give an averaged image of the particles at that height. Only signals well separated from each other and away from the image volume boundaries were included. This average at each height was deconvolved with a sphere of diameter 45 nm (the known fluorescent core size), yielding the measured PSF[82]. Both of

these steps were carried out using Huygens Professional deconvolution software (version 17.04, SVI).

Statistics and reproducibility

The particle sizes were expressed as the means and their poly-dispersities (the standard deviation over the mean diameter). The number of particles measured to obtain these values are specified in the methods section. The other results in this article were expressed as mean ± standard deviation.

Data availability

The data that support the findings of this study are available from the corresponding author upon reasonable request.

References

1. Pawley, J. *Handbook of Biological Confocal Microscopy*. (Springer, New York, 2010).
2. Vicidomini, G., Bianchini, P. & Diaspro, A. STED super-resolved microscopy. *Nat. Methods* **15**, 173–182 (2018).
3. Deng, S., Liu, L., Cheng, Y., Li, R. & Xu, Z. Effects of primary abberations on the fluorescence depletion patterns of STED microscopy. *Opt. Express* **18**, 1657–1666 (2010).
4. Booth, M., Andrade, D., Burke, D., Patton, B. & Zurauskas, M. Abberations and adaptive optics in super-resolution microscopy. *Microscopy* **64**, 251–261 (2015).
5. Shaw, P. J. & Rawlins, D. J. The point-spread function of a confocal microscope: its measurement and use in deconvolution of 3-D data. *J. Microsc.* **163**, 151–165 (1991).
6. Wallace, W., Schaefer, L. H. & Swedlow, J. R. A workingperson's guide to deconvolution in light microscopy. *BioTechniques* **31**, 1076–1097 (2001).
7. Li, Y. et al. Real-time 3D single-molecule localization using experimental point spread functions. *Nat. Methods* **15**, 367–369 (2018).
8. Chen, Y. et al. Measure and model a 3-D space-variant PSF for fluorescence microscopy image deblurring. *Opt. Express* **26**, 14375–14391 (2018).
9. Bierbaum, M., Leahy, B. D., Alemi, A. A., Cohen, I. & Sethna, J. P. Light microscopy at maximal precision. *Phys. Rev. X* **7**, 041007 (2017).
10. Leahy, B. D., Lin, N. & Cohen, I. Quantitative light microscopy of dense suspensions: colloid science at the next decimal. *Curr. Opin. Colloid Interface Sci.* **34**, 32–46 (2018).
11. Boddeke, F. R., van Vliet, L. J. & Young, I. T. Calibration of the automated z-axis of a microscope using focus functions. *J. Microsc.* **186**, 270–274 (1997).
12. Jensen, K. E., Weitz, D. A. & Spaepen, F. A three-dimensional calibration device for the confocal microscope. *Rev. Sci. Instrum.* **84**, 016018 (2013).
13. Bornfleth, H., Sätzler, K., Eils, R. & Cremer, C. High-precision distance measurements and volume-conserving segmentation of objects near and below the resolution limit in three-dimensional confocal fluorescence microscopy. *J. Microsc.* **189**, 118–136 (1998).
14. Besseling, T. H., Jose, J. & van Blaaderen, A. Methods to calibrate and scale axial distances in confocal microscopy as a function of refractive index. *J. Microsc.* **257**, 142–150 (2014).
15. Royon, A. & Converset, N. Quality control of fluorescence imaging systems: a new tool for performance assessment and monitoring. *Optik & Photonik* **12**, 22–25 (2017).
16. Corbett, A. D. et al. Microscope calibration using laser written fluorescence. *Opt. Express* **26**, 21887–21899 (2018).
17. Blom, H. & Widengren, J. Stimulated emission depletion microscopy. *Chem. Rev.* **117**, 7377–7427 (2017).
18. Cole, R. W., Jinadasa, T. & Brown, C. M. Measuring and interpreting point spread functions to determine confocal microscope resolution and ensure quality control. *Nat. Protoc.* **6**, 1929–1941 (2011).
19. Tortarolo, G., Castello, M., Diaspro, A., Koho, S. & Vicidomini, G. Evaluating image resolution in stimulated emission depletion microscopy. *Optica* **5**, 32–35 (2018).
20. Schmied, J. J. et al. DNA origami-based standards for quantitative fluorescence microscopy. *Nat. Protoc.* **9**, 1367–1391 (2014).
21. Scheckenbach, M., Bauer, J., Zähringer, J., Selbach, F. & Tinnefeld, P. DNA origami nanorulers and emerging reference structures. *APL Mater.* **8**, 110902 (2020).
22. Göttfert, F. et al. Strong signal increase in STED fluorescence microscopy by imaging regions of subdiffraction extent. *Proc. Natl. Acad. Sci. U.S.A.* **114**, 2125–2130 (2017).
23. Hanne, J. et al. STED nanoscopy with fluorescent quantum dots. *Nat. Commun.* **6**, 7127 (2015).
24. Yang, X. et al. Versatile application of fluorescent quantum dot labels in super-resolution fluorescence microscopy. *ACS Photonics* **3**, 1611–1618 (2016).
25. Urban, N. T., Willig, K. I., Hell, S. W. & Nägerl, U. V. STED nanoscopy of actin dynamics in synapses deep inside living brain slices. *Biophys. J.* **101**, 1277–1284 (2011).
26. Fouquet, C. et al. Improving axial resolution in confocal microscopy with new high refractive index mounting media. *PLoS One* **10**, 1–17 (2015).
27. Jiang, P., Bertone, J. F., Hwang, K. S. & Colvin, V. L. Single-crystal colloidal multilayers of controlled thickness. *Chem. Mater.* **11**, 2132–2140 (1999).
28. Uchic, M. D., Holzer, L., Inkson, B. J., Principe, E. L. & Munroe, P. Three-dimensional microstructural characterization using focused ion beam tomography. *MRS Bull.* **32**, 408–416 (2007).
29. van der Hoeven, J. E. S. et al. Bridging the gap: 3D real-space characterization of colloidal assemblies via FIB-SEM tomography. *Nanoscale* **11**, 5304–5316 (2019).
30. Lechner, W. & Dellago, C. Accurate determination of crystal structures based on averaged local bond order parameters. *J. Chem. Phys.* **129**, 114707 (2008).
31. Thijssen, J. H. J. Characterization of photonic colloidal crystals in real and reciprocal space. PhD thesis, Utrecht University (2007).
32. Mačković, M., Niekiel, F., Wondraczek, L. & Spiecker, E. Direct observation of electron-beam-induced densification and hardening of silica nanoballs by in situ transmission electron microscopy and finite element method simulations. *Acta Mater.* **79**, 363–373 (2014).
33. Hell, S., Reiner, G., Cremer, C. & Stelzer, E. H. K. Aberrations in confocal fluorescence microscopy induced by mismatches in refractive index. *J. Microsc.* **169**, 391–405 (1993).
34. Hell, S. & Wichmann, J. Breaking the diffraction resolution limit by stimulated emission: stimulated-emission-depletion fluorescence microscopy. *Opt. Lett.* **19**, 780–782 (1994).
35. Wildanger, D., Medda, R., Kastrup, L. & Hell, S. W. A compact STED microscope providing 3D nanoscale resolution. *J. Microsc.* **236**, 35–43 (2009).
36. Schermelleh, L. Super-resolution microscopy demystified. *Nat. Cell Biol.* **21**, 72–84 (2019).
37. Gustafsson, M. G. L. Three-dimensional resolution doubling in wide-field fluorescence microscopy by structured illumination. *Biophys. J.* **94**, 4957–4970 (2008).
38. Saxena, M., Eluru, G. & Gorthi, S. S. Structured illumination microscopy. *Adv. Opt. Photon.* **7**, 241–275 (2015).
39. Strack, R. Single-objective light sheet microscopy. *Nat. Methods* **18**, 28 (2021).
40. Sapoznik, E. A versatile oblique plane microscope for large-scale and high-resolution imaging of subcellular dynamics. *eLife* **9**, e57681 (2020).
41. Bea, S. W., Tan, W. & Hong, J. I. Fluorescent dye-doped silica nanoparticles: new tools for bioapplications. *Chem. Commun.* **48**, 2270–2282 (2012).
42. Bagwe, R. P. Optimization of dye-doped silica nanoparticles prepared using a reverse microemulsion method. *Langmuir* **20**, 8336–8342 (2004).
43. Wang, W. Volume labeling with Alexa Fluor dyes and surface functionalization of highly sensitive fluorescent silica (SiO_2) nanoparticles. *Nanoscale* **5**, 10369–10375 (2013).
44. Zhao, X., Bagwe, R. P. & Tan, W. Development of organic-dye-doped silica nanoparticles in a reverse microemulsion. *Adv. Mater.* **16**, 173–176 (2004).
45. Boonsin, R., Chadeyron, G., Roblin, J. P., Boyer, D. & Mahiou, R. Silica encapsulated fluorescein as a hybrid dye for blue-LED based lighting devices. *J. Mater. Chem. C* **4**, 6562 (2016).
46. Verhaegh, N. A. M. & van Blaaderen, A. Dispersions of rhodamine-labeled silica spheres: synthesis, characterization, and fluorescence confocal scanning laser microscopy. *Langmuir* **96**, 1427–1438 (1994).
47. Imhof, A. et al. Spectroscopy of fluorescein (FITC) dyed colloidal silica spheres. *J. Phys. Chem. B* **103**, 1408–1415 (1999).
48. Tovmachenko, O. G., Graf, C., van den Heuvel, D., van Blaaderen, A. & Gerritsen, H. C. Fluorescence enhancement by metal-core/Silica-shell nanoparticles. *Adv. Mater.* **18**, 91–95 (2006).
49. Urban, N. T., Foreman, M. R., Hell, S. W. & Sivan, Y. Nanoparticle-assisted STED nanoscopy with gold nanospheres. *ACS Photonics* **5**, 2574–2583 (2018).
50. de Mello Donegá, C. Synthesis and properties of colloidal heteronanocrystals. *Chem. Soc. Rev* **40**, 1512–1546 (2011).
51. Darbandi, M., Rhoman, R. & Nann, T. Single quantum dots in silica spheres by microemulsion synthesis. *Chem. Mater.* **17**, 5720–5725 (2005).

52. Koole, R. et al. On the incorporation mechanism of hydrophobic quantum dots in silica spheres by a reverse microemulsion method. *Chem. Mater.* **20**, 2503–2512 (2008).

53. van Hest, J. J. H. A. et al. Towards robust and versatile single nanoparticle fiducial markers for correlative light and electron microscopy. *J. Microsc.* **274**, 13–22 (2019).

54. Jeong, B. G. et al. Colloidal spherical quantum wells with near-unity photoluminescence quantum yield and suppressed blinking. *ACS Nano* **10**, 9297–9305 (2016).

55. Wang, N. et al. Highly luminescent silica-coated CdS/CdSe/CdS nanoparticles with strong chemical robustness and excellent thermal stability. *Nanotechnology* **28**, 185603 (2017).

56. Jin, D. et al. Nanoparticles for super-resolution microscopy and single-molecule tracking. *Nat. Methods* **15**, 415–423 (2018).

57. Tzeng, Y.-K. et al. Superresolution imaging of Albumin-conjugated Fluorescent nanodiamonds in cells by stimulated emission depletion. *Angew. Chem. Int. Ed.* **50**, 2262–2265 (2011).

58. Liu, Y. et al. Amplified stimulated emission in upconversion nanoparticles for super-resolution nanoscopy. *Nature* **543**, 229–233 (2017).

59. Lemén ager, G., De Luca, E., Sun, Y.-P. & Pompa, P. P. Super-resolution fluorescence imaging of biocompatible carbon dots. *Nanoscale* **6**, 8617–8623 (2014).

60. Bumb, A., Sarkar, S. K., Billington, N., Brechbiel, M. W. & Neuman, K. C. Silica encapsulation of fluorescent nanodiamonds for colloidal stability and facile surface functionalization. *J. Am. Chem. Soc.* **135**, 7815–7818 (2013).

61. Qian, H. S., Guo, H. C., Ho, P. C.-L., Mahendran, R. & Zhang, Y. Mesoporous-Silica-coated up-conversion fluorescent nanoparticles for photodynamic therapy. *Small* **5**, 2285–2290 (2009).

62. Lin, Y. et al. Tunable fluorescent silica-coated carbon dots: a synergistic effect for enhancing the fluorescence sensing of extracellular Cu^{2+} in rat brain. *ACS Appl. Mater. Interfaces* **7**, 27262–27270 (2015).

63. Demirörs, A. F., van Blaaderen, A. & Imhof, A. Synthesis of eccentric titania-silica core-shell and composite particles. *Chem. Mater.* **21**, 979–984 (2009).

64. Demirörs, A. F. et al. Seeded growth of titania colloids with refractive index tunability and fluorophore-free luminescence. *Langmuir* **27**, 1626–1634 (2011).

65. Jannasch, A., Demirörs, A. F., van Oostrum, P. D. J., van Blaaderen, A. & Schäffer, E. Nanonewton optical force trap employing anti-reflection coated, high-refractive-index titania microspheres. *Nat. Photon.* **6**, 469–473 (2012).

66. Hoogenboom, J. P. et al. Template-induced growth of close-packed and non-close-packed colloidal crystals during solvent evaporation. *Nano Lett.* **4**, 205–208 (2004).

67. Choy, T. C. *Effective medium theory: principles and applications.* (Oxford Univ. Press, Oxford, 2015).

68. Graf, C., Vossen, D. L. J., Imhof, A. & van Blaaderen, A. A general method to coat colloidal particles with silica. *Langmuir* **19**, 6693–6700 (2003).

69. Hagemans, F. Shaping Silica rods by tuning hydrolysis and condensation of Silica precursors. *Chem. Mater.* **31**, 521–531 (2019).

70. Osseo-Asare, K. & Arriagada, F. J. Preparation of SiO_2 nanoparticles in a non-ionic reverse micellar system. *Colloids and Surf.* **50**, 321–339 (1990).

71. Arriagada, F. J. & Osseo-Asare, K. Synthesis of nanosize silica in a nonionic water-in-oil microemulsion: effects of the water/surfactant Molar ratio and Ammonia concentration. *J. Colloid Interface Sci.* **211**, 210–220 (1999).

72. van Blaaderen, A. & Kentgens, A. P. M. Particle morphology and chemical microstructure of colloidal silica spheres made from alkoxysilanes. *J. Non-Cryst. Solids* **149**, 161–178 (1992).

73. Stöber, W., Fink, A. & Bohn, E. Controlled growth of monodisperse silica spheres in the micron size range. *J. Colloid Interface Sci.* **69**, 62–69 (1968).

74. Giesche, H. Synthesis of monodispersed silica powders I. Particle properties and reaction kinetics. *J. Eur. Ceram. Soc.* **14**, 189–204 (1994).

75. Giesche, H. Synthesis of monodispersed silica powders II. Controlled growth reaction and continuous production process. *J. Eur. Ceram. Soc.* **14**, 205–214 (1994).

76. van Blaaderen, A. Monodisperse colloidal Silica spheres from tetraalkoxysilanes: particle formation and growth mechanism. *J. Colloid Interface Sci.* **154**, 481–501 (1992).

77. Zhang, J., Liu, H., Wang, Z. & Ming, N. Assembly of high-quality colloidal crystals under negative pressure. *J. Appl. Phys.* **103**, 8–12 (2008).

78. Wong, S., Kitaev, V. & Ozin, G. A. Colloidal crystal films: advances in universality and perfection. *J. Am. Chem. Soc.* **125**, 15589–15598 (2003).

79. Meijer, J. M. et al. Self-assembly of colloidal cubes via vertical deposition. *Langmuir* **28**, 7631–7638 (2012).

80. García-Santamaría, F., Míguez, H., Ibisate, M., Meseguer, F. & López, C. Refractive index properties of calcined silica submicrometer spheres. *Langmuir* **18**, 1942–1944 (2002).

81. Schindelin, J. et al. Fiji: an open-source platform for biological-image analysis. *Nat. Methods* **9**, 676–682 (2012).

82. van der Voort, H. T. M. & Strasters, K. C. Restoration of confocal images for quantitative image analysis. *J. Microsc.* **178**, 165–181 (1995).

Acknowledgements

Author contributions

A.v.B. initiated the project. H.G. and A.v.B. supervised the research. J.F., C.L.K., and M.d.P. synthesized the particles. J.F., C.L.K., M.d.P., and E.B.v.d.W. performed the refractive index measurements. J.F. determined the fluorophore labeling density of the particles. J.F., M.d.P., E.B.v.d.W., and P.N.A.S. prepared the colloidal crystals. E.B.v.d.W., C.L.K., M.d.P., and P.N.A.S. performed the confocal (STED) microscopy measurements. D.A.M.d.W. performed the FIB-SEM measurements. E.B.v.d.W., J.F., H.G., and A.v.B. co-wrote the paper. All authors discussed the results and commented on the paper.

Competing interests

The authors declare no competing interests.

Additional information

Supplementary information The online version contains supplementary material available at https://doi.org/10.1038/s42003-021-02432-3.

Correspondence and requests for materials should be addressed to A.v.B.

Peer review information *Communications Biology* thanks Aurel Barbotin and the anonymous reviewer(s) for their contribution to the peer review of this work. Primary Handling Editors: Marco Fritzsche and Anam Akhtar.

Reprints and permission information is available at http://www.nature.com/reprints

Publisher's note Springer Nature remains neutral with regard to jurisdictional claims in published maps and institutional affiliations.